Spin-induced linear polarization of photoluminescence in antiferromagnetic van der Waals crystals

Xingzhi Wang¹*, Jun Cao¹, Zhengguang Lu^{2, 3}, Arielle Cohen⁴, Hikari Kitadai¹, Tianshu Li⁴, Qishuo Tan¹, Matthew Wilson⁵, Chun Hung Lui⁵, Dmitry Smirnov², Sahar Sharifzadeh^{1, 4, 6, 7}, Xi Ling^{1, 4, 8} *

¹ Department of Chemistry, Boston University, Boston, Massachusetts 02215, USA.

² National High Magnetic Field Laboratory, Tallahassee, Florida 32310, USA.

³ Department of Physics, Florida State University, Tallahassee, Florida 32306, USA.

⁴ Division of Materials Science and Engineering, Boston University, Boston, Massachusetts 02215, USA.

⁵ Department of Physics and Astronomy, University of California, Riverside, California 92521, USA

⁶ Department of Electrical and Computer Engineering, Boston University, Boston, Massachusetts 02215, USA.

⁷ Department of Physics, Boston University, Boston, Massachusetts 02215, USA.

⁸ The Photonics Center, Boston University, Boston, Massachusetts 02215, USA.

^{*}To whom the correspondence should be addressed. Email address: xzwang@bu.edu; xzwang@bu.edu; xzwang@bu.edu;

Abstract

Antiferromagnets are promising components for spintronics due to their terahertz resonance, multilevel states, and absence of stray fields. However, the zero net magnetic moment of antiferromagnets makes the detection of the antiferromagnetic order and the investigation of fundamental spin properties notoriously difficult. Here, we report an optical detection of Néel vector orientation through an ultra-sharp photoluminescence in the van der Waals antiferromagnet NiPS3 from bulk to atomically thin flakes. The strong correlation between spin flipping and electric dipole oscillator results in a linear polarization of the sharp emission, which aligns perpendicular to the spin orientation in the crystal. By applying an in-plane magnetic field, we achieve manipulation of the photoluminescence polarization. This correlation between emitted photons and spins in layered magnets provides new routes for investigating magneto-optics in two-dimensional materials, and hence opens a path for developing opto-spintronic devices and antiferromagnet-based quantum information technologies.

Since the discovery of monolayer ferromagnets, magneto-optics plays a compelling role in revealing new physics of magnetism in the extreme nanoscale limit¹⁻³. For example, the spin orientation in two-dimensional (2D) ferromagnets can be detected using the magneto-optical Kerr effect (MOKE)^{1,2} or spontaneous circularly polarized photoluminescence (PL)⁴. Compared to ferromagnets, however, the studies of magneto-optics in 2D antiferromagnets are far more difficult due to the lack of net magnetic moments^{5,6}, despite their appealing natures for next-generation spintronic devices⁷⁻¹². Raman spectroscopy¹³⁻¹⁵ and second harmonic generation (SHG)^{16,17} have been applied to detect the presence of spin structure in 2D antiferromagnets, based on the expansion of unit cell and the breaking of the centrosymmetry of materials. Nevertheless, these methods are not sufficient to provide fine information of spin properties in 2D antiferromagnets, such as the local Néel vector orientation¹³⁻¹⁶. One promising strategy to investigate the spin properties in 2D antiferromagnet is to leverage a coupling between spins and other excitation elements, which do not rely on the stray fields of spins.

Monolayer NiPS₃ crystal has hexagonal lattice structure with three-fold rotation symmetry, thus it is reasonable to exhibit distinctive in-plane isotropic properties (Supplementary Fig. 1a)^{18,19}. Such in-plane isotropy is largely retained in monoclinic bulk NiPS₃ due to the weak interlayer coupling, though the interlayer stacking order in principle breaks the three-fold rotation symmetry^{15,18}. For instance, bulk NiPS₃ exhibits similar isotropic Raman response as the monolayers¹⁵. However, when NiPS₃ transitions from the paramagnetic phase to the antiferromagnetic phase across its Néel temperature ($T_N \sim 152$ K), the spins are aligned either in parallel or antiparallel along the in-plane *a*-axis with a small out-of-plane component as shown in Fig. 1a²⁰. In each single layer, both the spin orientation and the zigzag ferromagnetic chains differ the *a*-axis from the other two directions rotated by $\pm 120^{\circ}$, and hence breaks the three-fold rotation symmetry. The Néel vector (i.e. antiferromagnetic vector) in the antiferromagnets is defined as $L = M_1 - M_2$, where M_1 and M_2 represent two oppositely aligned spins (Fig. 1b). As a consequence, the Néel vector in NiPS₃ also orients mainly along *a*-axis of the lattice.

Here, we report an observation of spin-correlated PL in van der Waals (vdW) antiferromagnetic NiPS₃ from bulk to trilayer flakes. The PL peak exhibits excellent monochromaticity with a near-intrinsic linewidth (~330 μeV at temperature T ~ 5 K) in the near-infrared range (with photon energy of ~1.476 eV). Notably, the sharp emission shows a linear polarization correlated to the Néel vector orientation of NiPS₃, supported by the temperature and magnetic-field dependent spectroscopic study. Such a spin-correlated emission demonstrated in our study allows us to expediently read the spin properties in bulk and atomically thin NiPS₃ flakes using steady-state spectroscopy, and provides new concepts in the design of novel opto-spintronics in 2D systems.

Ultra-sharp emission from antiferromagnetic NiPS₃

Atomically thin NiPS₃ flakes are mechanically exfoliated from the high-quality NiPS₃ bulk single crystals (Fig. 1c and Supplementary Fig. 1). Fig. 1d shows a typical PL spectra of bulk and trilayer NiPS₃ under 568-nm continuous-wave laser excitation at $T \sim 5$ K. A distinctly sharp peak (labeled as X) is resolved at ~ 1.476 eV in the spectra of both the bulk and trilayer samples. The trilayer PL energy is only slightly (~ 0.8 meV) higher than the bulk PL energy, and both are close to the band gap energy (~ 1.5 eV) of NiPS₃^{18,21}. In

contrast, such a sharp emission is absent in bilayer flakes (Supplementary Fig. 2a). Here we focus on peak X, while other peaks in close proximity are discussed in the Supplementary Section 5 and 6. The intensity of peak X clearly decreases with the increase of temperature and vanishes at T > 120 K, which is ~ 30 K lower than the T_N of NiPS₃ (Fig. 2a). Moreover, as the temperature decreases from 120 to 20 K, the integrated PL intensity exhibits gradual variation (Fig. 2b). This behavior of peak X is distinct from most of phenomena induced by magnetic phase transition, which usually follow an exponential function and exhibit a non-differentiable inflection point at $T_N^{13,14}$. Our experimental results imply that the disappearance of peak X at a high temperature is not directly caused by the magnetic phase transition. The measured time-resolved decay curve of peak X, after deconvolution with the instrument response function, indicates an upper bound of the lifetime of ~10 ps (Supplementary Fig. 3d). As a comparison, peak X exhibits a full width at half maximum (FWHM) of ~330 μ eV, corresponding to a lower limit for lifetime of ~2 ps. Therefore, the lifetime of peak X is estimated in the order of picoseconds.

As one of the appealing features, the exceptionally narrow linewidth of peak X raises concern over whether the emission originates from isolated structural defects in the crystal (inset in Fig 1d)²². However, this possibility can be ruled out based on the linear dependence of PL intensity on the excitation power up to 2.5 mW (Fig. 2c)²³ and the emission homogeneity over several micrometers area on the flakes with same thickness (Supplementary Fig. 3c)²⁴⁻²⁶. Particularly, we observed an absorption peak at ~ 1.480 eV, which is close to the PL peak X at ~ 1.476 eV (Fig. 2d). These two peaks exhibit similar temperature dependence, suggesting they share a similar origin (Supplementary Fig. 4). The noticeable absorption also strongly excludes isolated defect states as the origin of the emission, as the corresponding absorption is generally invisible due to the limited density of states in crystals²³.

In addition, our data reveals a correlation between the sharp peak X with both the magnetic and electronic properties of NiPS₃, further suggesting it stems from an intrinsic transition of the material. First, the layer-dependent data shows that the PL intensity rapidly decreases with the reduction of layer-number in the few-layer region, and finally disappears in the bilayer sample (Supplementary Fig. 2). The suppression of PL intensity in thin flakes

could be the consequence of the suppression of magnetic ordering, which has been previously established¹⁵. Second, peak X locates near the absorption edge ($\sim 1.5 \text{ eV}$) of NiPS₃, referring that it is possibly correlated to the band edge transition of the material. The calculated electronic band structure, from density functional theory (DFT) including a Hubbard U parameter on the Ni atoms, indicates an indirect band gap of 1.55 eV in bulk NiPS₃ (Supplementary Fig. 5). The density of states shows that the low-lying conduction band is mainly composed of Ni d-orbital electrons, while the high-lying valence bands are predominated by S p-orbital electrons. Therefore, we speculate that peak X originates from the transition involving these two types of electrons in NiPS₃. A recent investigation reporting a similar phenomenon from NiPS₃ attributes the sharp emission to a transition between a Zhang-Rice triplet and a Zhang-Rice singlet²⁷. Such a transition represents a variation of the relative spins between the holes in Ni d-orbital and S p-orbital, i.e., the relative spins between the unpaired electrons in Ni d-orbital and S p-orbital 27,28 , aligning well with our speculation. However, it remains ambiguous, but fundamentally important to understand why an intrinsic transition can generate such a narrow emission at hundreds of μeV . We consider this feature is possibly a consequence of the trapped states in the crystal due to a self-doping effect (see Supplementary Section 4).

Linearly polarized PL in the antiferromagnetic phase

More importantly, since NiPS₃ is a vdW crystal with intrinsic antiferromagnetism, the observation of sharp emission provides an excellent platform for studying magneto-optics in quasi-2D systems. Specifically, it is extremely intriguing to explore whether peak X could couple to the spin structure in the material to great extent. To this end, we have measured the polarization-dependent PL of NiPS₃ in two configurations (Supplementary Fig. 7). In the first configuration, we rotate the incident laser polarization (P_{in}) and measure the total PL intensity of peak X with a fixed collection polarization (P_{col}). We do not observe clear dependence of the PL on P_{in} (Fig. 3a). The isotropy of the PL intensity is due to the weak anisotropy of optical absorption above the band gap energy. In the second configuration, we maintain the same excitation laser polarization, while collect PL of peak X at different polarization (P_{col}). Remarkably, we find that the collected PL varies significantly with P_{col} (Fig. 3a). The PL intensity reaches the maximum (minimum) when

 P_{col} is perpendicular (parallel) to the a-axis, which is determined by the selected-area electron diffraction (SAED) (Supplementary Fig. 8). From bulk down to few-layer samples, a similar phenomenon is observed and the PL intensity can be fitted by a sinusoidal function: $I(\theta) = I_0 + I_1 \sin^2 \theta$, where θ is the angle between the PL polarization and the a-axis of NiPS₃; I_0 and I_1 are fitting constants (dashed lines in Fig 3a and Supplementary Fig. 9).

To investigate the origin of the linear polarization, we first conduct the temperature dependent PL polarization measurement (Fig. 3b). We define the PL linear polarization degree, $\rho = (I_b - I_a)/(I_b + I_a)$, where I_a (I_b) is the PL peak intensity when P_{col} is parallel to the a-axis (b-axis). We find that ρ is ~ 70 % at T < 70 K, and drops significantly with increasing temperature (Fig. 3c). The temperature dependent PL polarization degree is fitted well by $\rho(T) \sim \left|1 - \frac{T}{T_N}\right|^{2\beta_{PL}}$, where β_{PL} is a critical exponent indicating the decay trend near the phase transition temperature³¹. We obtain $\beta_{PL} = 0.26 \pm 0.05$, which is in good agreement with β =0.23 \sim 0.26 for the temperature-dependent magnetic intensity in 2D XY systems^{29,30}. This accordance suggests that the linear polarization of peak X in NiPS₃ arises from the ordered spins.

As shown in Fig 1a, the anisotropic spin structure of NiPS3 is mainly contributed by two factors – Néel vector orientation and ferromagnetic spin chain direction, which are both along the a-axis. It becomes a fundamental question over which one gives rise to the linear polarization of peak X. As peak X is reported to originate from the transition between a Zhang-Rice triplet and a Zhang-Rice singlet, the relative spin orientation of the unpaired electrons in Ni d-orbital and S p-orbital changes from the same to the opposite direction during the transition²⁷. Since the initial spins of unpaired electrons are known to be along the a-axis of crystal, the spin-flipping causes a spin quantum number difference ΔS along the a-axis. Therefore, the generated electric dipole should be rotating in the plane perpendicular to the a-axis, thus emits photon carries an angular momentum J along the a-axis to conserve the total quantum number in this direction. Meanwhile, this electric dipole will emit photons in the equatorial plane with a linear polarization perpendicular to the polar direction (Fig. 3d). As a result, in our case of NiPS3, peak X exhibits a linear

polarization perpendicular to the Néel vector when we collect the signal along the surface normal.

In the presence of spin-photon coupling, it is of great significance to investigate the magneto-optical properties of NiPS₃ cross $T_N \sim 152$ K. Unfortunately, peak X vanishes at a characteristic temperature of ~ 120 K, which is ~ 30 K below the T_N. Nevertheless, the optical absorption of NiPS₃ also exhibits clear anisotropy near the band edge (~1.5 eV) in the antiferromagnetic phase (Fig. 3e). Linear dichroism (LD) of NiPS₃ is obtained by the formula $LD = (A_a - A_b)/(A_a + A_b)$, where $A_a (A_b)$ is the absorptance when the polarization of the incident white light is parallel to the a-axis (b-axis) (Fig. 3f). LD keeps around 12% when T < 70 K and dramatically decays with temperature increasing. Moreover, LD reaches a minimum around T_N, inferring the anisotropy of the absorption arises from the anisotropic spin structure. The temperature-dependent LD is fitted by $LD(T) \sim \left| 1 - \frac{T}{T_{N}} \right|^{2\beta_{LD}}$, where $\beta_{LD} = 0.28 \pm 0.04$ matches well with β_{PL} and reported β in other 2D XY spin systems^{31,32}. Magnetic linear dichroism is a common phenomenon in many ferromagnetic and antiferromagnetic materials with spins aligning in-plane³¹. Due to the magneto-optical effect, the optical absorption coefficient changes for different light polarizations. Consequently, the electric field of transmitted and reflected light is suppressed along the spin orientation, resulting in a weak polarization for depolarized light or Voigt effect for linear polarized light³². The magnetic linear dichroism near the band edge and PL linear polarization observed in NiPS₃ crystals indicates that its spin-structure strongly regulates the optical transition. A magnetic linear dichroism of ~12% in NiPS₃ is rather strong, compared to that in common magnetic materials, where the magnetic linear dichroism is typically smaller than 1%^{32,33}. In particular, peak X features an even larger polarization degree $\sim 70\%$, suggesting a significantly strong coupling to spins. Additionally, the PL spectra in the range of 1.35 - 1.5 eV show distinct polarized characters at different emission energies, in stark opposition that the linear polarization of PL peaks stems from the anisotropic reabsorption of the material (Supplementary Fig. 10).

Magnetic manipulation of emitted photons

Although the temperature-dependent study provides remarkable evidence that the linear polarization of peak X arises from the spin structure, the underlying mechanism of the coupling between transition and spin is still controversial²⁷. Especially, the fact that the ferromagnetic spin chain and the Néel vector align along the same direction (i.e., a-axis) leads to the notorious difficulty on identifying their contributions to the polarization of peak X experimentally. Based on the XY-nature of spins in NiPS₃ at low temperature, one strategy to elucidate this complication is to apply an in-plane field to rotate the Néel vector away from the spin chain direction²⁰. As shown in the model we proposed, when the Néel vector rotates in the ab-plane, the spin-flipping should result in ΔS along the new direction of Néel vector, which is away from the a-axis (Fig. 4a). Meanwhile, the generated dipole oscillator remains perpendicular to the ΔS vector. Therefore, the polarization of peak X also rotates away from the b-axis, with the same angle of Néel vector rotation. We conduct a magneto-optical study on NiPS₃ in the Voigt geometry. We mount two bulk NiPS₃ samples (labeled as S₁ and S₂) inside a magnetic cell. Their crystal orientations (i.e. a-axis) are rotated by 120° relative to each other (Fig. 4b). As a result, the PL polarization of peak X from sample S₁ and S₂ xis off by 120° at zero applied magnetic field (Fig. 4c), consistent with our results in Fig. 3a. Then, we apply an in-plane magnetic field (B) up to 14 T along the a-axis of S_1 (which is 120° away from the a-axis of S_2), and conduct the polarized PL measurements (Fig. 4c). Remarkably, we achieve the manipulation of the polarization of the sharp emission. The polarization of peak X from S₂ shows a clear rotation with the increase of the magnetic field and finally orients in the same direction as the PL polarization from S_1 at B = 14 T. The result provides another unambiguous evidence that the polarization peak X is determined by the spin structures, rather than the weak crystalline anisotropy from the layer stacking.

We compare the PL polarization angles φ_1 and φ_2 for sample S_1 and S_2 at different B-fields (Fig. 4d). After excluding the effect from Faraday rotation, φ_1 remains unchanged at ~ 0 degree in the whole magnetic field range from 0 to 14 T. However, φ_2 continuously rotates when applied field increases in the range of $0 \sim 10$ T and $11 \sim 14$ T, while dramatically changes at $B = \sim 10.5$ T. Since the ferromagnetic spin chain can only align along the zigzag directions of the crystal, the hexagonal lattice structure of NiPS₃ limits the minimum rotation of spin chain to 60° , which is labeled as horizontal black dashed lines

in Fig. 4d. In contrast, the Néel vector in NiPS₃ is able to align along any directions in the plane as we observed in the experiments due to its XY behavior at low temperature¹⁵. We also notice, if the spin chains could rotate with a step of 60° in small magnetic domains, a collective effect in the region of the laser spot would also result in a continuous rotation of PL polarization due to an increasing percentage of domain areas with changed spin chain. However, this possibility cannot be achieved, since such an intermediate phase containing multiple spin chain states would cause a reduction of the polarization degree, which is in contradiction to the unchanged polarization degree of S2 from 0 to 9 T observed in our measurements (Fig. 4e). The sudden drop of the polarization degree at ~10.5 T indicates a field-induced magnetic phase transition from an antiferromagnetic state to another antiferromagnetic state, similar to the case in MnPS₃^{34,35}. Therefore, our magneto-optical measurements provide unambiguous evidence that the polarization of peak X is determined by the Néel vector direction instead of the spin chain direction in NiPS₃.

Conclusion

Benefiting from the spin-correlated emission in NiPS₃, the Néel vector orientation can be optically detected as perpendicular to the PL polarization. Even though the manipulation of the PL polarization was only demonstrated in bulk NiPS₃, we anticipate similar results on few-layer flakes, in which the linearly polarized emission has also been demonstrated (Supplementary Fig. 9). Our report on the spin-correlated PL in vdW antiferromagnets – NiPS₃ will greatly advance future fundamental researches in magnetism and magnetooptics. Most of the prior optical spin-probe techniques for antiferromagnets are technically difficult to conduct and not suitable for ultrathin samples, since they require an ultrafast laser to induce the thermal or magnetic perturbation^{33,36}, and the amplitudes of signals are proportional to the thickness of samples^{5,33}. In contrast, the spin-induced polarization of PL demonstrated here using a steady-state micro-spectroscopy method offers an easy, fast, nondestructive strategy to determine the Néel vector orientation and investigate the spin properties of atomically thin antiferromagnets. We anticipate the conceptually new mechanism of spin-photon coupling will stimulate future theoretical and experimental studies in the field, promoting the development of opto-spintronic device and magnetic quantum information technology.

References

- Huang, B. *et al.* Layer-dependent ferromagnetism in a van der Waals crystal down to the monolayer limit. *Nature* **546**, 270-273 (2017).
- Gong, C. *et al.* Discovery of intrinsic ferromagnetism in two-dimensional van der Waals crystals. *Nature* **546**, 265-269 (2017).
- Burch, K. S., Mandrus, D. & Park, J.-G. Magnetism in two-dimensional van der Waals materials. *Nature* **563**, 47-52 (2018).
- 4 Seyler, K. L. *et al.* Ligand-field helical luminescence in a 2D ferromagnetic insulator. *Nat. Phys.* **14**, 277-281 (2018).
- Němec, P., Fiebig, M., Kampfrath, T. & Kimel, A. V. Antiferromagnetic optospintronics. *Nat. Phys.* **14**, 229-241 (2018).
- Jungwirth, T., Marti, X., Wadley, P. & Wunderlich, J. Antiferromagnetic spintronics. *Nat. Nanotechnol.* **11**, 231-241 (2016).
- 7 Kirilyuk, A., Kimel, A. V. & Rasing, T. Ultrafast optical manipulation of magnetic order. *Rev. Mod. Phys.* **82**, 2731-2784 (2010).
- 8 Kampfrath, T. *et al.* Coherent terahertz control of antiferromagnetic spin waves. *Nat. Photonics* **5**, 31-34 (2011).
- 9 Kriegner, D. *et al.* Multiple-stable anisotropic magnetoresistance memory in antiferromagnetic MnTe. *Nat. Commun.* 7, 11623 (2016).
- Olejník, K. *et al.* Antiferromagnetic CuMnAs multi-level memory cell with microelectronic compatibility. *Nat. Commun.* **8**, 15434 (2017).
- 11 Marti, X. *et al.* Room-temperature antiferromagnetic memory resistor. *Nat. Mater.* **13**, 367 (2014).
- Wadley, P. *et al.* Electrical switching of an antiferromagnet. *Science* **351**, 587-590 (2016).
- Wang, X. *et al.* Raman spectroscopy of atomically thin two-dimensional magnetic iron phosphorus trisulfide (FePS₃) crystals. *2D Mater.* **3**, 031009 (2016).
- Lee, J.-U. *et al.* Ising-Type Magnetic Ordering in Atomically Thin FePS₃. *Nano Lett.* **16**, 7433-7438 (2016).
- 15 Kim, K. *et al.* Suppression of magnetic ordering in XXZ-type antiferromagnetic monolayer NiPS₃. *Nat. Commun.* **10**, 345 (2019).

- 16 Chu, H. *et al.* Linear Magnetoelectric Phase in Ultrathin MnPS₃ Probed by Optical Second Harmonic Generation. *Phys. Rev. Lett.* **124**, 027601 (2020).
- Sun, Z. *et al.* Giant nonreciprocal second-harmonic generation from antiferromagnetic bilayer CrI₃. *Nature* **572**, 497-501 (2019).
- Du, K. *et al.* Weak Van der Waals Stacking, Wide-Range Band Gap, and Raman Study on Ultrathin Layers of Metal Phosphorus Trichalcogenides. *ACS Nano* **10**, 1738-1743 (2016).
- 19 Kuo, C.-T. *et al.* Exfoliation and Raman Spectroscopic Fingerprint of Few-Layer NiPS₃ Van der Waals Crystals. *Sci. Rep.* **6**, 20904 (2016).
- Wildes, A. R. *et al.* Magnetic structure of the quasi-two-dimensional antiferromagnet NiPS₃. *Phys. Rev. B* **92**, 224408 (2015).
- Piacentini, M., Khumalo, F. S., Olson, C. G., Anderegg, J. W. & Lynch, D. W. Optical transitions, XPS, electronic states in NiPS₃. *Chemical Physics* **65**, 289-304 (1982).
- Liu, X. & Hersam, M. C. 2D materials for quantum information science. *Nature Reviews Materials* **4**, 669-684 (2019).
- Schmidt, T., Lischka, K. & Zulehner, W. Excitation-power dependence of the near-band-edge photoluminescence of semiconductors. *Phys. Rev. B* **45**, 8989-8994 (1992).
- Gao, W. B., Fallahi, P., Togan, E., Miguel-Sanchez, J. & Imamoglu, A. Observation of entanglement between a quantum dot spin and a single photon. *Nature* **491**, 426-430 (2012).
- Jungwirth, N. R. & Fuchs, G. D. Optical Absorption and Emission Mechanisms of Single Defects in Hexagonal Boron Nitride. *Phys. Rev. Lett.* **119**, 057401 (2017).
- Tonndorf, P. et al. Single-photon emitters in GaSe. 2D Mater. 4, 021010 (2017).
- Kang, S. *et al.* Coherent many-body exciton in van der Waals antiferromagnet NiPS₃. *Nature* **583**, 785-789 (2020).
- Zhang, F. C. & Rice, T. M. Effective Hamiltonian for the superconducting Cu oxides. *Phys. Rev. B* **37**, 3759-3761 (1988).

- Bramwell, S. T. & Holdsworth, P. C. W. Magnetization and universal sub-critical behaviour in two-dimensional XY magnets. *J. Phys. Condens. Matter.* **5**, L53-L59 (1993).
- Bramwell, S. T., Day, P., Hutchings, M. T., Thorne, J. R. G. & Visser, D. Neutron scattering and optical study of the magnetic properties of the two-dimensional ionic rubidium chromium bromide chloride ferromagnets Rb₂CrCl₃Br and Rb₂CrCl₂Br₂. *Inorganic Chemistry* **25**, 417-421 (1986).
- Ferre, J. & Gehring, G. A. Linear optical birefringence of magnetic crystals. *Reports on Progress in Physics* **47**, 513-611 (1984).
- Tesařová, N. *et al.* Systematic study of magnetic linear dichroism and birefringence in (Ga,Mn)As. *Phys. Rev. B* **89**, 085203 (2014).
- Saidl, V. *et al.* Optical determination of the Néel vector in a CuMnAs thin-film antiferromagnet. *Nat. Photonics* **11**, 91-96 (2017).
- Chittari, B. L. *et al.* Electronic and magnetic properties of single-layer MPX₃ metal phosphorous trichalcogenides. *Phys. Rev. B* **94**, 184428 (2016).
- Long, G. *et al.* Persistence of Magnetism in Atomically Thin MnPS₃ Crystals. *Nano Lett.* **20**, 2452-2459 (2020).
- Kimel, A. V. *et al.* Ultrafast non-thermal control of magnetization by instantaneous photomagnetic pulses. *Nature* **435**, 655-657 (2005).
- 37 Kim, S. Y. *et al.* Charge-Spin Correlation in van der Waals Antiferromagnet NiPS₃. *Phys. Rev. Lett.* **120**, 136402 (2018).

Methods

Sample preparation. NiPS₃ single crystals were grown using a chemical vapor transport (CVT) method¹⁸. A stoichiometric amount of high-purity elements (mole ratio Ni:P:S = 1:1:3, around 1 g in total) and iodine (about 10-20 mg) as a transport agent were sealed into a quartz ampule and kept in a two-zone furnace (650–600 °C). The length of the quartz ampule was about 16 cm with a 13 mm external diameter. The pressure inside the ampule was pumped down to 1×10^{-4} Torr. After 1 week of heating, the ampule was cooled down to room temperature with bulk crystals in the lower temperature end. The purity of the synthesized sample has been confirmed by series of characterizations. The powder X-Ray diffraction (PXRD) data was collected on a Bruker D8 Discover diffractometer with Cu Ka radiation of $\lambda = 1.5418$ Å at 40 kV and 40 mA. Elemental analysis experiments were conducted using energy dispersive spectroscopy (EDS) attached to a field emission scanning electron microscope (FESEM, Zeiss Supra 55). Transmission electron microscopy (TEM) measurements were performed on a FEI Tecnai Osiris transmission electron microscope, operating at a 200 keV accelerating voltage. Selected-area electron diffraction (SAED) were measured on a JEOL 2100 transmission electron microscope. The SAED simulation was perform through STEM CELL software.

Few-layer NiPS₃ flakes were prepared on Si substrates with 285-nm SiO₂ layer by mechanical exfoliation from a bulk single-crystal. The morphology and thickness of exfoliated flakes were characterized using an optical microscopy (Nikon DS-Ri2) and atomic force microscopy (Bruker Dimension 3000) in a tapping mode.

Raman scattering, PL and absorptance spectroscopy. Optical measurements were carried out on a micro-Raman spectrometer (Horiba-JY T64000) and the signal was collected through a 50× long-working-distance objective. A cryostat (Cryo Industry of America, USA) was used to provide a vacuum environment and a continuous temperature from 5 to 300 K by liquid helium flow. Raman scattering measurement was perform using a triple-grating mode with 1800 g/mm gratings, and a 568-nm laser line from a Kr⁺/Ar⁺ ion laser (Coherent Innova 70C Spectrum) was used to excite the sample. Micro-PL and micro-absorption measurements were carried out using a single-grating mode. For PL, 458- and 568-nm laser lines from the Kr⁺/Ar⁺ ion laser (Coherent Innova 70C Spectrum) were used

to excite the sample. The backscattered signal was dispersed with a 150 g/mm or 1800 g/mm grating. A stabilized tungsten-halogen white-light source (SLS201L, Thorlabs) was used to irradiate the bulk sample from the bottom in micro-absorption measurements. The signal from an effective area $\sim 5 \, \mu m$ in diameter was collected. The absorptance spectra were determined by $A(\lambda) = 1 - T(\lambda)/T_0(\lambda)$, where $T(T_0)$ is the intensity of light transmit through the sample (substrate).

Polarization-dependent PL and magneto-PL measurement. The polarization-dependent PL and magneto-PL experiment were performed in the National High Magnetic Field Lab (NHMFL). In the polarization-dependent PL measurement, a 488-nm laser was used to excite the bulk crystal and exfoliated flakes. A 50× long-working-distance objective was used to focus the excitation onto the sample and collect the PL signal. The magneto-optical experiments were performed with 14 T DC magnet on bulk crystal. A 532-nm continuous-wave laser was used to excite the sample. The sample was vertically put inside the magnetic cell with the surface parallel to the applied magnetic field. A mirror was set between objective and sample with 45° to change the optical path by 90°. A 10× objective was used to focus excitation onto the sample and collect the PL signal. For both the polarization-dependent and magnetic-field-dependent experiment, the PL signal was filtered by an analyzer, subsequently collected by a multi-mode optical fiber and measured by a spectrometer with a CCD camera (Princeton Instruments, IsoPlane 320).

Time-resolved PL measurement. Time-resolved PL experiment was conducted using a time-correlated single photon counting technique. The excitation laser pulses came from an oscillator (Light Conversion Inc., Pharos) with 1030 nm output wavelength, 80 MHz repetition rate, and 90 fs pulse duration. The second harmonic (515 nm wavelength) of the laser was used to excite the samples. The PL signal was spectrally dispersed and filtered by a grating monochromator before detection by a photodiode.

DFT calculation. DFT calculations were performed using the Vienna Ab Initio Simulation Package (VASP)³⁸⁻⁴¹. We utilized the local density approximation (LDA) with a Hubbard U parameter of 4.0 eV on each Nickel atom^{34,37} to describe the correlated behavior of the d electrons, using the simplified, rotationally invariant Dudarev approach implemented in VASP⁴². Projector augmented wave (PAW) potentials describe the core and nuclei of

atoms, with 10, 5 and 6 electrons treated explicitly for Ni, P and S respectively^{43, 44}. The k-point mesh for self-consistent field and structural optimization was 4×7×5, sufficient to converge the total energy to 1 meV/atom. Additionally, for structural optimization we used a cutoff energy for the planewave basis set of 470 eV and a threshold of 1 meV/Angstrom for all forces. To determine the magnetic state of the NiPS₃, we initialized the system with two types of antiferromagnetic and one ferromagnetic state, with an initial magnetic moment of 3.0 or -3.0 assigned to each nickel atom and determined the lowest energy structure. In agreement with previous studies, we found that antiferromagnetically coupled "zigzag" stripes of aligned spins described in Fig. 1a were the lowest energy structure⁴⁵. The other structures considered were a ferromagnetic configuration and an antiferromagnetic configuration in which spins alternated between nearest neighbors.

To calculate the band structure and density of states, we used a k-path between 12 high-symmetry points in the Brillouin zone⁴⁶ with 10 k-points along each segment (or 20, when considering spin-orbit coupling). We checked the effect of spin-orbit coupling by performing non-collinear magnetic structure calculations in VASP⁴⁷ starting from both the DFT relaxed geometry and the lattice parameters from experiment. In both cases, spin-orbit coupling resulted in narrow band splitting (< 0.01 eV) in some segments of the valance and conduction bands.

- 38. Kresse, G. & Hafner, J. Ab Initio Molecular Dynamics for Liquid Metals. *Phys. Rev. B* 47 (1), 558–561, (1993).
- 39. Kresse, G. & Hafner, J. Ab Initio Molecular-Dynamics Simulation of the Liquid-Metal--Amorphous-Semiconductor Transition in Germanium. *Phys. Rev. B* **49** (20), 14251–14269, (1994).
- Kresse, G. & Furthmüller, J. Efficiency of Ab-Initio Total Energy Calculations for Metals and Semiconductors Using a Plane-Wave Basis Set. *Comput. Mater. Sci.* 6 (1), 15–50, (1996).
- 41. Kresse, G. & Furthmüller, J. Efficient Iterative Schemes for Ab Initio Total-Energy Calculations Using a Plane-Wave Basis Set. *Phys. Rev. B* **54** (16), 11169–11186, (1996).

- 42. Dudarev, S. L., Botton, G. A., Savrasov, S. Y., Humphreys, C. J. & Sutton, A. P. Electron-Energy-Loss Spectra and the Structural Stability of Nickel Oxide: An LSDA+U Study. *Phys. Rev. B* **57** (3), 1505–1509, (1998).
- 43. Kresse, G. & Hafner, J. Norm-Conserving and Ultrasoft Pseudopotentials for First-Row and Transition Elements. *J. Phys. Condens. Matter* **6** (40), 8245–8257, (1994).
- 44. Kresse, G. & Joubert, D. From Ultrasoft Pseudopotentials to the Projector Augmented-Wave Method. *Phys. Rev. B* **59** (3), 1758–1775, (1999).
- 45. Kurita, N. & Nakao, K. Band Structure of Magnetic Layered Semiconductor NiPS₃. *J. Phys. Soc. Jpn.* **58** (1), 232–243, (1989).
- 46. Setyawan, W. & Curtarolo, S. High-Throughput Electronic Band Structure Calculations: Challenges and Tools. *Comput. Mater. Sci.* **49** (2), 299–312, (2010).
- 47. Steiner, S. et al. Calculation of the Magnetic Anisotropy with Projected-Augmented-Wave Methodology and the Case Study of Disordered Fe_{1-x}Co_x Alloys. *Phys. Rev. B* **93** (22), 224425, (2016).

Data availability

The data represented in Figs. 1–4 are provided with the paper as source data. All other data that support results in this article are available from the corresponding author on reasonable request.

Acknowledgements

This material is based upon work supported by the National Science Foundation (NSF) under Grant No.(1945364). X.W. and X.L. acknowledge the financial support from Boston University and the Boston University Photonics Center. The TEM imaging was performed at the Center for Nanoscale Systems (CNS), a member of the National Nanotechnology Coordinated Infrastructure Network (NNCI), which is supported by the National Science Foundation under NSF award no. 1541959. CNS is part of Harvard University. A.C. and S.S. acknowledge financial support from the U.S. Department of Energy (DOE), Office of Science, Basic Energy Sciences (BES) Early Career Program under Award No. DESC0018080. The authors acknowledge the computational resources

through the Extreme Science and Engineering Discovery Environment (XSEDE), which is supported by National Science Foundation grant number ACI-1548562; and the National Energy Research Scientific Computing Center, a DOE Office of Science User Facility supported by the Office of Science of the U.S. Department of Energy under Contract No. DE-AC02-05CH11231. Z.L. and D.S. acknowledge support from the U.S. Department of Energy (No. DE-FG02-07ER46451) for National High Magnetic Field Laboratory, which is supported by National Science Foundation through NSF/DMR-1644779 and the State of Florida.

Author contributions

X.W. and X.L. conceived the experiment. X.W. carried out PL and absorption measurements. X.W., J.C., and Z.L. conducted the magneto-PL measurements with the assistance from D.S. at the National High Magnetic Field Laboratory. J.C. and X.W. prepared samples. J.C., H.K., T.L., and Q.T. carried out the sample characterization. A.C. and S.S. performed theoretical calculations. M.W. performed the time-resolved PL measurement under the supervision of C.H.L. X.W. and X.L. performed the analysis and interpretation of the data. All authors assisted in the interpretation of data and contributed to the writing of the manuscript.

Competing Interests

The authors declare no competing interests.

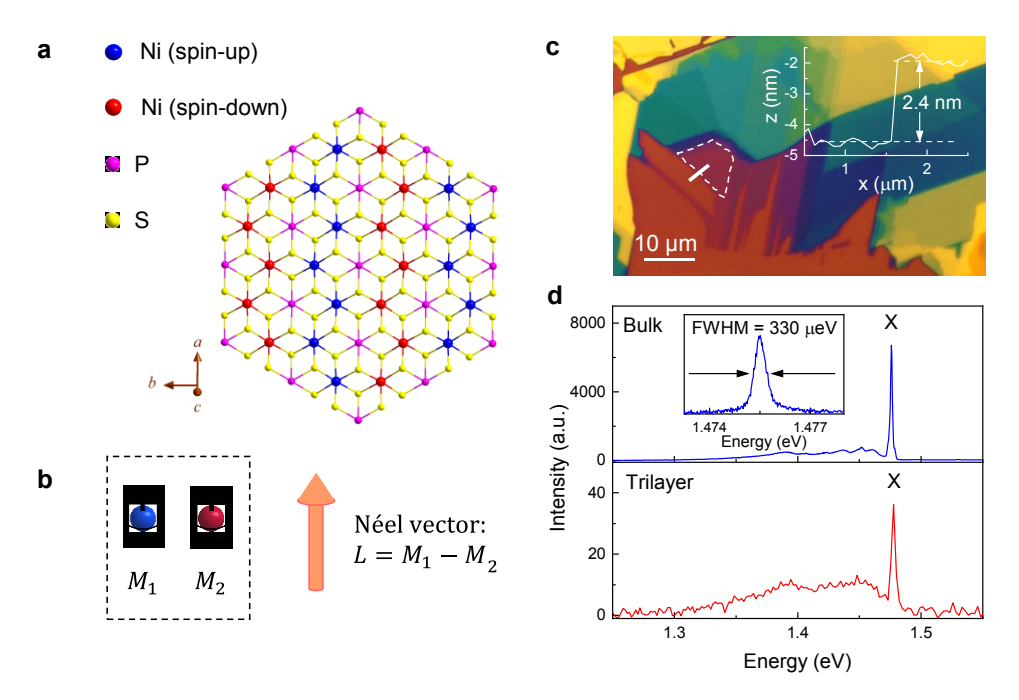


Fig. 1 | **Antiferromagnetic spin structure and sharp emission of NiPS₃. a**, Top view of spin structure of vdW antiferromagnet NiPS₃. The crystal orientations (a-, b- and c-axes) are labelled by brown arrows. The spin orientation is mainly along a-axis of the crystal. **b**, Schematic illustration of Néel vector, defined as $L = M_1 - M_2$, where M_1 and M_2 represent two oppositely aligned spins, respectively. **c**, Optical microscopy image of exfoliated NiPS₃ flakes on a silicon substrate with 285-nm SiO₂ layer, where different colors represent the samples with different thickness. The scale bar is 10 μm. The trilayer flake is marked by the white dashed line and the inset is its height profile along the white solid line. **d**, PL spectra from bulk and the trilayer NiPS₃ flake under 568-nm continuous-wave laser excitation at 5 K. The sharp PL peak is labelled as X. The inset shows a high-resolution spectrum of peak X with a full width at half maximum (FWHM) of ~330 μeV in bulk NiPS₃.

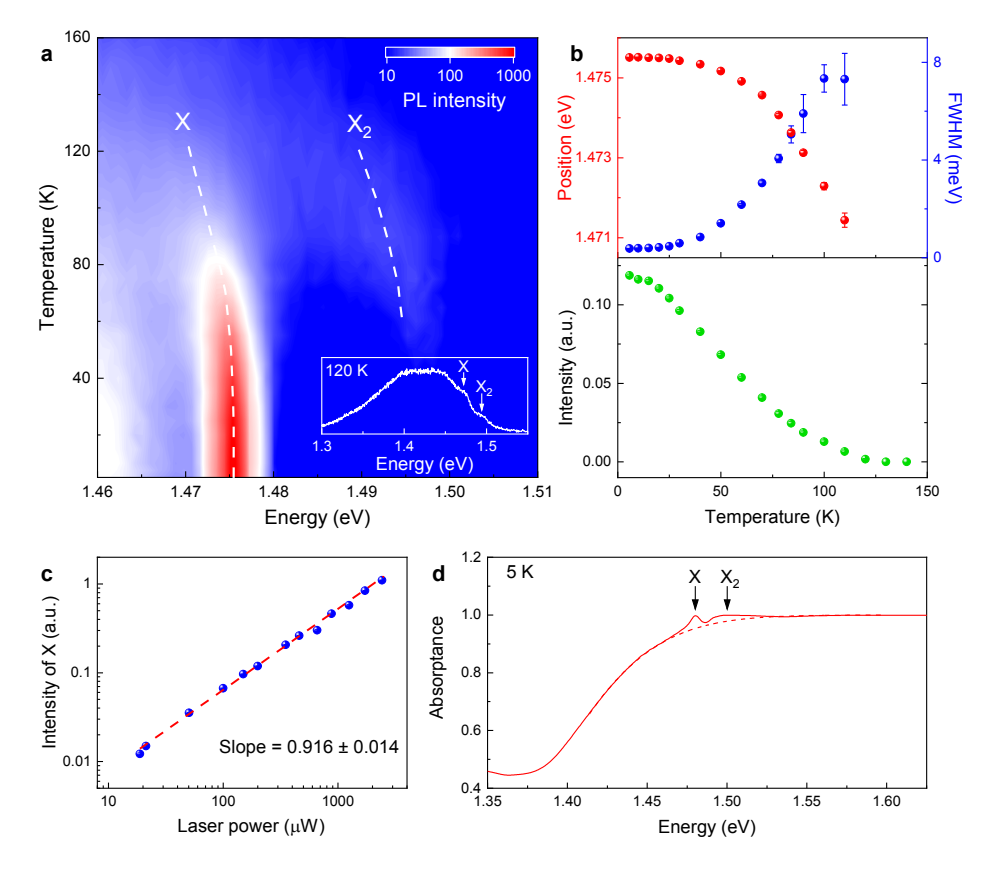


Fig. 2 | **Characterization of sharp peak X in NiPS₃. a**, Temperature-dependent PL color map under 568-nm laser excitation. Two PL peaks (labelled as X and X_2) are observed. The inset is the spectrum at 120 K. **b**, Extracted FWHM, peak position and integrated intensity of peak X as a function of temperature under 568-nm excitation. **c**, Excitation-power dependent intensity of peak X excited by a 568-nm laser. The slope of linear fitting indicates the linear dependence of intensity on the excitation power in the range from 17 μ W to 2.5 mW. **d**, Absorptance spectrum of bulk NiPS₃ at 5 K. Two absorption peaks locating at the band edge are assigned to the X and X₂.

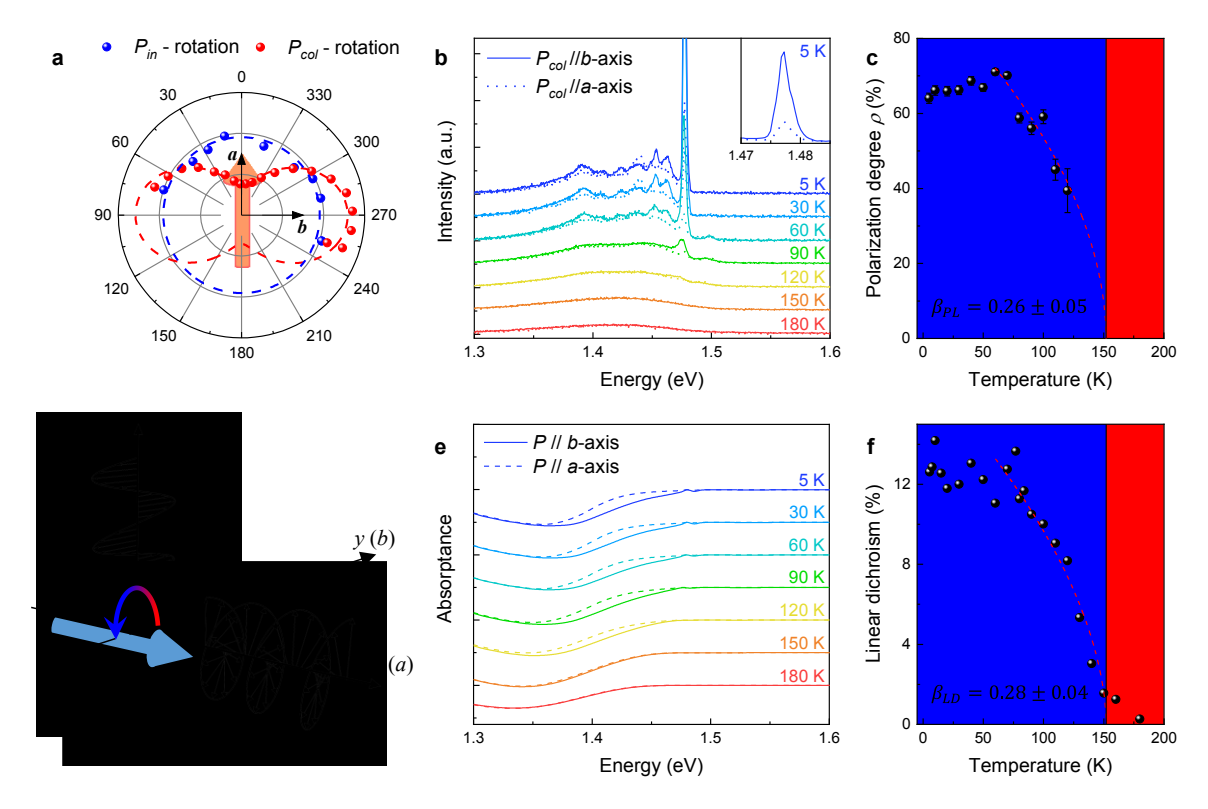


Fig. 3 | Spin-induced linear polarization of PL and absorption anisotropy in NiPS₃. a. PL intensity as a function of the incident laser polarization (blue) and collection polarization (red) at 5 K. The crystal orientations (a- and b-axes) and Néel vector orientation have been labeled by black thin and orange thick arrows, respectively. b, Temperature-dependent PL spectra in two polarization configurations under 568-nm excitation. The inset shows the linear polarization of peak X at 5 K. c, PL polarization degree $(\rho = (I_b - I_a)/(I_b + I_a))$ as a function of temperature. The dash line is the fitting using formula, $\rho(T) \sim \left| 1 - \frac{T}{T_N} \right|^{2\beta_{PL}}$, where $\beta_{PL} = 0.26 \pm 0.05$. **d**, Schematic illustration of origin of linear polarization of peak X. The spin flipping from red to blue thick arrows along x activates an electric dipole oscillation in vz-plane, which generates circular polarized photons along x-direction and linear polarized photons along z-direction. e, Temperature-dependent absorptance spectra of NiPS3 bulk crystal in two polarization configurations. f, Linear dichroism $(LD = (A_a - A_b)/(A_a + A_b))$ as a function of temperature. The dash line is the fitting using formula, $LD(T) \sim \left| 1 - \frac{T}{T_N} \right|^{2\beta_{LD}}$, where $\beta_{LD} = \frac{T}{T_N} \left| \frac{dt}{dt} \right|^{2\beta_{LD}}$ 0.28 ± 0.04 . The blue and red areas in (c) and (f) represent the antiferromagnetic (AFM) and the paramagnetic (PM) phase, respectively.

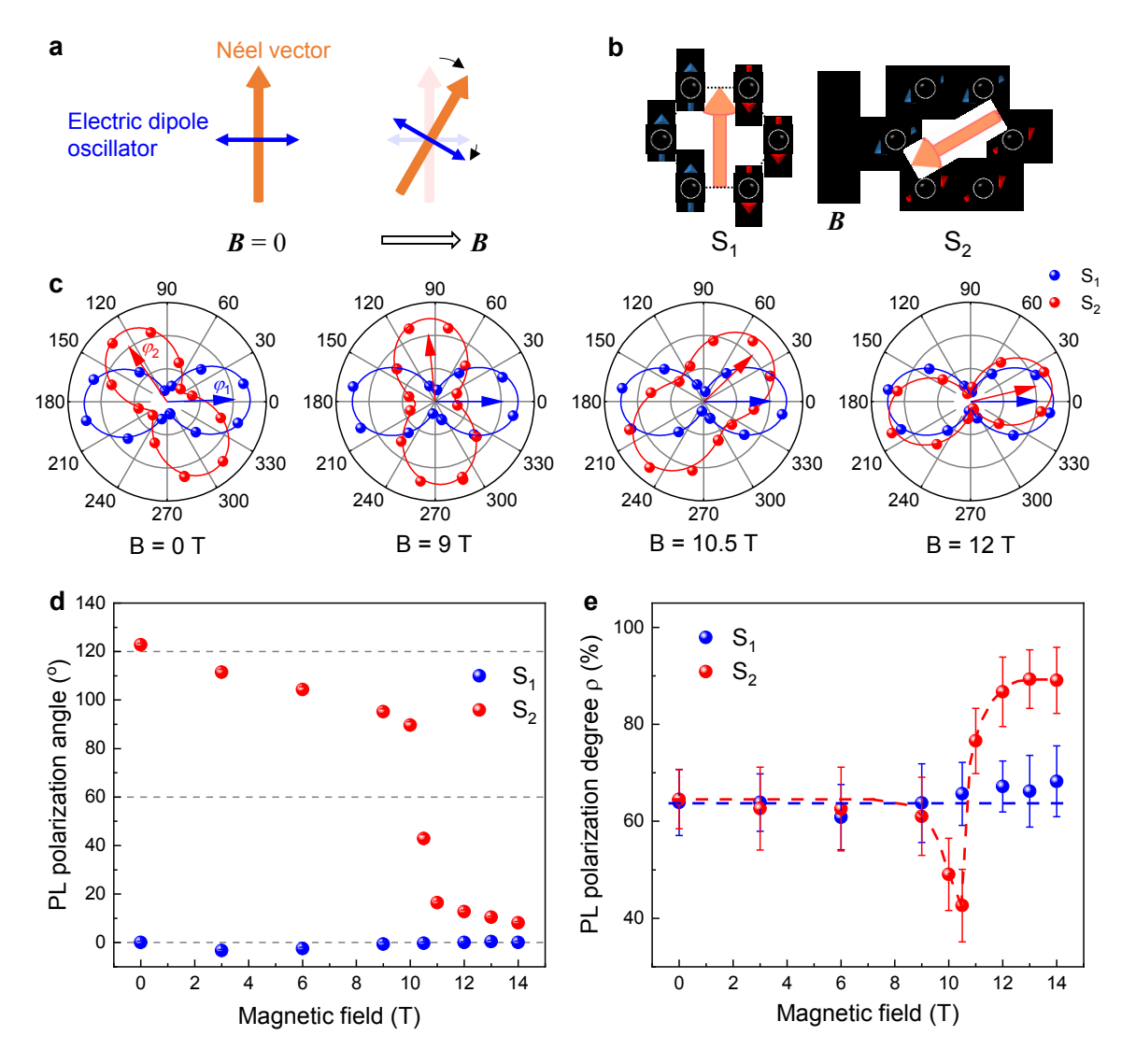


Fig. 4 | **Magnetic manipulation of PL polarization in the Voigt geometry. a**, Illustration of rotating linear polarization of peak X in an applied in-plane field. The orange solid, blue solid and black hollow arrows represent the direction of Néel vector, electric dipole oscillator and applied field, respectively. **b**, Illustrated diagram of the initial alignments of spins (blue and red thin arrows) and Néel vectors (orange thick arrows) in two samples, with respect to the direction of the in-plane magnetic field (hollow thick arrow). The crystal orientations (i.e. a-axis) of two bulk NiPS₃ samples (S₁ and S₂) are 120° from each other. **c**, Integrated PL intensity of peak X as a function of collection polarization angle on S₁ and S₂ at different magnetic field (B = 0, 9, 10.5 and 12 T). φ_1 and φ_2 labelled in the first panel are the PL polarization angle of sample S₁ and S₂, with respect to the direction of applied magnetic field. **d**, PL polarization angle φ_1 (φ_2) of sample S₁ (S₂) as a function of in-plane magnetic field. The black dash lines are the possible zigzag spin chain directions. **e**, Polarization degree, $\rho = (I_b - I_a)/(I_b + I_a)$, as a function of applied magnetic field for S₁ and S₂. The results show a magnetic phase transition around B = 10.5 T.